# Effect of Niobium on the Defect Chemistry and Oxidation Kinetics of Tetragonal ZrO$_2$

Uuganbayar Otgonbaatar, Wen Ma, Mostafa Youssef, and Bilge Yildiz*

Laboratory for Electrochemical Interfaces, Department of Nuclear Science and Engineering, Massachusetts Institute of Technology, 77 Massachusetts Avenue, Cambridge, Massachusetts 02139, United States

ABSTRACT: Zirconium−niobium alloys are currently proposed for applications in water-cooled nuclear reactors. However, the mechanisms by which Nb impacts the corrosion resistance of these alloys are yet to be clarified. In this work, we utilize a thermodynamic framework informed by density functional theory calculations to predict the effect of Nb on the equilibria of charged defects in tetragonal ZrO$_2$, and discuss how the changes in the defect concentrations affect the protectiveness of this oxide that grows natively on Zr alloys during oxidation. Our analysis shows that Nb dissolves predominantly in the oxidation state 5+ as a substitutional defect on the Zr sublattice, with charge compensation achieved by the negatively charged Zr vacancies. Moreover, Nb dissolution is limited to the oxygen-rich conditions, i.e., in the oxide surface facing oxidizing environment. We validate this finding by performing X-ray photoelectron spectroscopy on oxidized Zr−Nb alloys. The introduction of Nb in tetragonal ZrO$_2$ is found to enhance the concentration of Zr vacancies and of free electrons and to decrease the concentration of oxygen vacancies. We conclude that the net effect of Nb on the corrosion kinetics of Zr alloys is favorable if the rate limiting process is oxygen transport, while Nb would be detrimental if electron transport limits the oxidation kinetics.
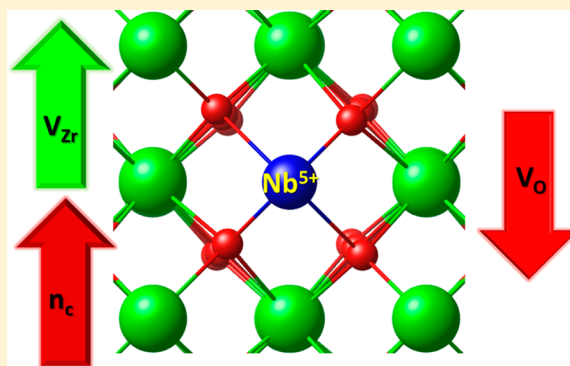
1. INTRODUCTION

Zirconia (ZrO$_2$) is among the most important metal oxides because of its wide range of applications.[1] Its applications span fuel cells,[2] thermal barrier coating,[3] and protection against the corrosion of nuclear fuel cladding in water-cooled nuclear reactors.[4−6] Furthermore, zirconia is used in biomedical hip implants[7] and dental restorations[8] and recently it was suggested as a gate dielectric for metal oxide semiconductor devices.[9] This richness in zirconia's applications can be traced back to its high strength and fracture toughness,[10] its high dielectric constant,[9] and the possibility of significantly enhancing its ionic conductivity via doping[11] and straining.[12,13] Properties of zirconium oxide in all these applications, as in the larger family of oxides, are affected by the equilibria and the structure of intrinsic (native) and extrinsic charged defects. For example, the protectiveness of the native zirconium oxide layer against fast corrosion of zirconium alloys is governed by the concentration and mobility of anion, cation, and electronic defects. While the specific aim of the current work is to assess the effect of an extrinsic defect, niobium (Nb) dopant, on the defect equilibria and charge transfer properties of tetragonal ZrO$_2$ (T-ZrO$_2$) in the context of protectiveness against corrosion, the approach and findings reported here are more broadly applicable to other applications of zirconia as well.

Traditional corrosion resistant zirconium alloys have Fe, Cr, and possibly Ni in composition,[14] whereas modern zirconium alloys have varying content of Nb ranging from 1.0 to 2.5 wt %.[15] Despite the indication from alloy designers that higher Nb content is correlated with improved corrosion resistance,[4] there have been conflicting experimental reports on the effect of Nb on corrosion kinetics.[15−17] Some corrosion experiments conducted in a simulated light water reactor environment over extended times undoubtedly point to the superior performance of Nb containing alloys compared to alloys in which Zr is alloyed by Fe, Cr, and Ni.[4] However, fundamental experimental efforts which attempted to find a correlation between the better corrosion performance and Nb content have resulted in no clear conclusion.[15] Yilmazbayhan et al. conducted corrosion weight gain measurements on Zr based alloys with varying Nb content (0.4−2.5 wt % Nb) while keeping other constituents constant but eventually did not identify a clear correlation between Nb content and corrosion kinetics.[15] Similar work by Yueh et al. also produced inconclusive results.[17] On the contrary, there are experiments even indicating that Nb containing alloys exhibit poor corrosion performance compared to traditional alloys during the initial stages of corrosion.[16]

Corrosion protectiveness is impacted by intrinsic chemical and electronic properties, microstructure, and mechanical stability of the oxide layer that forms natively on metallic alloys.[6,18] In this paper, we focus on assessing how the intrinsic chemical and electronic properties of the zirconia layer that

forms on zirconium alloys are impacted by the presence of Nb. Thermodynamically, ZrO_2 is stable in the monoclinic phase at ambient pressure and up to 1440 K.[19] At higher temperatures, the tetragonal phase is stable. However, experiments indicate the presence of a large fraction of the tetragonal phase close to the metal/oxide interface in nuclear reactor operation temperature ($\sim$600 K).[4] The stabilization of the tetragonal phase at such low temperatures was attributed to the large compressive stress exerted on the oxide due to the lattice mismatch between the metal and the oxide.[20] Moreover, the part of the oxide where there is enrichment in tetragonal ZrO_2 is believed to be coherent and intact and hence protective.[4] Thus, in this work, we focus on the effect of Nb on tetragonal ZrO_2.

The intrinsic defect chemistry of T-ZrO_2 has been studied in our recent work;[21] however, the impact of Nb on the defect equilibria in T-ZrO_2 is yet to be elucidated. Nb can exhibit various oxidation states when present as a dopant in the oxide. There is disagreement in the literature on the charge state of Nb in ZrO_2. X-ray absorption near-edge structure (XANES) K-edge measurements conducted by Froideval et al. concluded that the Nb charge state falls between 2+ and 4+ and that the 5+ charge state of Nb is not present in the ZrO_2 layer grown on Zr alloys.[22] However, many authors assume a stable Nb^{5+} charge state in ZrO_2.[23,24] As the previous experiments did not provide conclusive evidence to describe either the correlation between Nb content and corrosion of the alloys or the nature of the Nb impurity defect in the oxide, we aim here to resolve these questions by first principle simulations coupled with some validation experiments. In particular, we quantify the effect of Nb on the defect equilibria in tetragonal zirconia while clarifying the dominant oxidation state of Nb in T-ZrO_2.

Corrosion of Zr alloys proceeds via the point-defect mediated diffusion of oxygen and zirconium through the oxide layer.[6,14] It was also hypothesized that electron transport plays an important role in the corrosion of Zr and of Zr-based alloys.[14] Both the diffusion of point defects and the electron transport are directly proportional to their respective concentrations. Thus, we take the first step in fundamentally understanding the corrosion of Zr and its alloys, by determining the concentration of point and electronic defects in the protective oxide, i.e., in this case taken as the T-ZrO_2. Recently, we assessed the equilibrium concentration of the intrinsic point and electronic defects in tetragonal zirconia.[21] In the current work, we quantitatively assess the effect of Nb, present initially as an alloying element in the Zr alloy and subsequently as an oxidized impurity in tetragonal ZrO_2, on the equilibrium concentration of point and electronic defects in the oxide. The goal is to understand the impact of Nb in ZrO_2 on net corrosion rate by altering the concentration of ionic and electronic defects.

We constructed a Kröger–Vink diagram for Nb-doped tetragonal ZrO_2 while taking into account finite temperature effects, based on our theoretical approach informed by density functional theory (DFT) calculations.[21] Our results indicate that Nb is present predominantly in the form of a substitutional defect (substituting the host Zr^{4+}) and in the oxidation state 5+. The presence of Nb leads to an increase in the concentrations of the zirconium vacancies in 4– charge state and of free electrons and to a decrease in the concentration of the oxygen vacancies in 2+ charge state. All these trends were found in the high oxygen partial pressure regime corresponding to the oxide/water or oxide/oxygen gas interface in a corrosion scenario. We expect that the decrease in the oxygen vacancy concentration should slow down the corrosion rate, whereas the increase in electrons should accelerate the corrosion rate. The net effect of Nb depends on which of these two defects (oxygen vacancies and free electrons) is the rate limiting in oxidation kinetics. Our theoretical predictions are in part validated by experiments, where both are in qualitative agreement, suggesting Nb enrichment at the oxygen-rich region of the oxide (i.e., near its surface).

The organization of the rest of this paper is as follows. First, we summarize the theoretical framework to calculate the defect equilibria in Nb-doped T-ZrO_2, the details of the DFT calculations, and the experimental details to quantify the near-surface composition (Nb content) of the oxide by using X-ray photoelectron spectroscopy. Second, we present the results of both the computational and experimental approaches. Third, we discuss the implications of the results in relation to the corrosion of Zr alloyed with Nb. Finally, we give concluding remarks and recommendations for future work.

2. METHODS

2.1. Theoretical Approach. In this section, we summarize the framework of computing defect formation energies in an insulator, the representation of the defect equilibria in the form of a Kröger–Vink diagram, and our approach in analyzing the defect electronic and atomic structures. More details can be found in our work on the native defects of T-ZrO_2.[21] In this work, we adopt Kröger–Vink notation for denoting the defects. For example, $Nb_{Zr}^{\bullet}$ represents a Nb ion sitting on a Zr site (substitutional) with an effective charge of (+) with respect to the original ion which is Zr^{4+}. It follows that the formal charge of Nb in this case is (5+).

2.1.1. Defect Energetics. The details of computing the formation energy of a defect in a material with a band gap can be found in refs 21 and 25. Here we summarize the important notions exemplified on a Nb substitutional defect. The formation energy of the defect Nb_{Zr}^q can be expressed as in eq 1

$$\Delta E^f(Nb_{Zr}^q) = E^{DFT}(Nb_{Zr}^q) - E_{ZrO_2}^{DFT} + \mu_{Zr} - \mu_{Nb}$$
$$+ q(E_{VBM} + \mu_F) + E_{MP} \tag{1}$$

where $E^{DFT}(Nb_{Zr}^q)$ and $E_{ZrO_2}^{DFT}$ are the DFT energies of the defective and defect-free supercells, respectively. E_{VBM} denotes the energy of the valence band maximum in the defect-free supercell. μ_{Zr} and μ_{Nb} are the chemical potentials of zirconium and niobium, respectively. μ_F represents the chemical potential of electrons which is also known as the Fermi level. Finally, E_{MP} is the leading term of the Makov–Payne correction for the spurious interactions arising from applying periodic boundary conditions.[26] This correction was shown to perform reasonably well for the native and hydrogen defects in T-ZrO_2.[21,27]

The oxygen chemical potential μ_O is defined in terms of the oxygen partial pressure P_{O_2} as in eq 2

$$2\mu_O(T, P_{O_2}) = \mu_{O_2}(T, P_{O_2})$$
$$= E_{O_2}^{DFT} + \mu_{O_2}^0(T, P^0) + k_B T \ln\left(\frac{P_{O_2}}{P^0}\right) \tag{2}$$

where $E_{O_2}^{DFT}$ is the energy of an isolated O_2 molecule as calculated by DFT. $\mu_{O_2}^0(T, P_{O_2})$ is the difference in the chemical potential of O_2 between $T = 0$ K and the temperature of

interest at a reference pressure P^0 which is set to 1 atm. $\mu_{O_2}^0(T, P_{O_2})$ was extracted from tabulated thermochemical data.[28] The chemical potential of zirconium was expressed as in eq 3

$$\mu_{Zr} = E_{ZrO_2}^{DFT} - 2\mu_O \qquad (3)$$

In this work, we set the chemical potential of Nb to be independent of P_{O_2}. This fixed value was calculated as

$$\mu_{Nb}(T) = E_{NbO}^{DFT} - \mu_O(T, P_{O_2} = 1 \text{ atm}) \qquad (4)$$

with E_{NbO}^{DFT} representing the DFT calculated energy of the NbO chemical formula. The choice of NbO as a reference to calculate μ_{Nb} is due to a literature-based suggestion that during the oxidation of Zr–Nb alloys in steam at temperatures close to reactor operation (600 K) both NbO and NbO$_2$ form but Nb$_2$O$_5$ does not form.[29] Since our calculations here are performed at a much higher temperature (1500 K), we expect a more reduced form of Nb oxide, that is, NbO, to be thermodynamically favored. Therefore, we adopted NbO here as the reference state of Nb oxide. It should be noted that there is a possibility of a compound in the form Zr$_x$Nb$_y$O$_z$ to be produced during Zr–Nb oxidation and if confirmed experimentally it would be a more appropriate reference state for μ_{Nb}. However, in the absence of such experimental confirmation and because of a lack of NbO–ZrO$_2$ and NbO$_2$–ZrO$_2$ phase diagrams, it is not possible to guess a physically justifiable chemical formula or a crystal structure for such a compound.

Equation 1 describes the formation energy of the defects at 0 K with the exception of oxygen chemical potential. The latter was obtained from thermochemical tables, and thus, it includes finite temperature effects. However, as we showed previously,[21] the finite temperature effects in the solid crystal impact the free energy of formation of the defects. The dominant contribution is due to phonons, and that is included here. A secondary contribution is due to the band electronic entropy, and this one was not included in this work.

To measure the stability of a defect complex with respect to dissociation into its constituents, we calculated its binding energy following the definition in ref 27. The defect complex of interest in this work is Nb$_{Zr}^q$ which can dissociate into a Zr vacancy and an interstitial Nb. For this complex, the binding energy reads

$$E_{bind}(Nb_{Zr}^q) = \max[\Delta E^f(Nb_{Zr}^q) - \Delta E^f(Nb_i^{q_1}) \\ - \Delta E^f(V_{Zr}^{q-q_1})] \qquad (5)$$

Per this definition, a negative binding energy indicates a stable complex. The association of Nb$_{Zr}^q$ with native defects such as oxygen vacancies and interstitials was found to be very unlikely (large positive binding energy), and hence, such complexes are excluded from discussion in this work.

2.1.2. Constructing Kröger–Vink Diagram. A Kröger–Vink diagram for a metal oxide is an isothermal representation of the defect concentration as a function of P_{O_2}. The procedures described in detail in ref 21 to construct this diagram were adopted here in combination with the new ingredient added in this work which is Nb defects. The DFT calculated band gap for T-ZrO$_2$ is 3.9 eV. In ref 21, it was shown that applying a rigid shift for the DFT calculated conduction band by 0.3 eV to match the experimental band gap of 4.2 eV[30] results in native defect equilibria in good agreement with prior electrical

conductivity measurements.[31] Thus, a similar rigid shift was applied here too.

2.1.3. Defect Electronic and Atomic Structure. In this study, we focus on analyzing the electronic and atomic structure of Nb defects in T-ZrO$_2$. Interstitial Nb defects were found to have a very high formation energy, and thus, the analysis was limited to the substitutional defects. On a substitutional site, we examined various formal oxidation states for Nb starting from 5+ to 0 which correspond to effective charges ranging from 1+ to 4−. This was achieved by varying the number of electrons in the simulation supercell followed by ionic relaxation. However, as extensively discussed in the literature, it is not always possible to achieve all charge states due to electron or hole delocalization into the bands.[27,32,33] To decide which achievable charge states Nb can take on a substitutional site (i.e., without delocalization), we employed several analytical approaches. First, Bader charge analysis[34] was used to determine the charge on each ion in the DFT supercell using the code developed by Henkelman et al.[35] Charge delocalization is evidenced by negligible change in the calculated Bader charge on Nb ion when an electron is inserted or removed from the simulation supercell. Second, we examined the net electronic spin density localized on each ion as another indication for charge localization. In the rest of the paper, we focus on the charge states which were possible to localize on Nb. Finally, we calculated the electronic density of states for the oxidation states of Nb substitutional defects which were deemed to be achievable.

2.2. Computational Details. Total energy calculations were performed using the projector augmented wave method[36] in the density functional theory framework. The Perdew, Burke, and Ernzerhof (PBE)[37,38] exchange-correlation functional as implemented in the Vienna *Ab Initio* Simulation Package (VASP)[39−42] was employed. The adequacy of the standard PBE functional to describe tetragonal zirconia was discussed in our previous work.[21] However, Nb as a transition metal dopant in an oxide with band gap can have multiple oxidation states as discussed above. Standard PBE may fail in properly localizing the d electrons needed to describe these multiple oxidation states. To overcome this issue, we applied an *intra*-atomic onsite Coulomb interaction term (the so-called U term) to the d electrons of Nb. We adapted a value of 1.5 eV for the U term from ref 43. In addition, we employed the rotationally invariant version of DFT+U suggested by Dudarev et al.[44] In comparing the results of PBE and PBE+U, we found both of them to stabilize the oxidation states 3+, 4+, and 5+ of Nb on a zirconium site. The main impact of the U term is to increase the formation energy of the 5+ oxidation state. In what follows, we present results using PBE+U.

A Monkhorst–Pack 2 × 2 × 2 k-point mesh is used for reciprocal space sampling. Plane wave expansion is cut off at a kinetic energy of 450 eV. Ionic relaxation was considered converged when the forces on all ions were less than 0.01 eV/Å. The convergence criterion for electronic free energy was set to 10^{-4} eV. The host T-ZrO$_2$ simulation supercell consists of 96 atoms, and point defect and defect complexes were added to the host supercell in their respective calculations. DFT calculations were performed to simulate the dilute defect concentration limit, and hence, the supercell volume was fixed. The electronic density of states of the achievable oxidation states of Nb substitutional defects were calculated using a k-point mesh of 6 × 6 × 6 centered at the gamma point in

Table 1. Calculated Bader Charge, Net Spin, and Assigned Formal Oxidation States and Spin States for the Three Achievable Charge States of Nb Substitutional Defect

Nb defect	Nb'_{Zr}	Nb^x_{Zr}	$Nb^{\bullet}_{Zr}$
Bader charge on Nb (e)	+2.0	+2.3	+2.6
net spin on Nb/net cell spin (μ_B)	1.8/1.9	0.9/1.0	0.0/0.0
formal oxidation state/spin state	Nb^{3+}/triplet	Nb^{4+}/doublet	Nb^{5+}/singlet
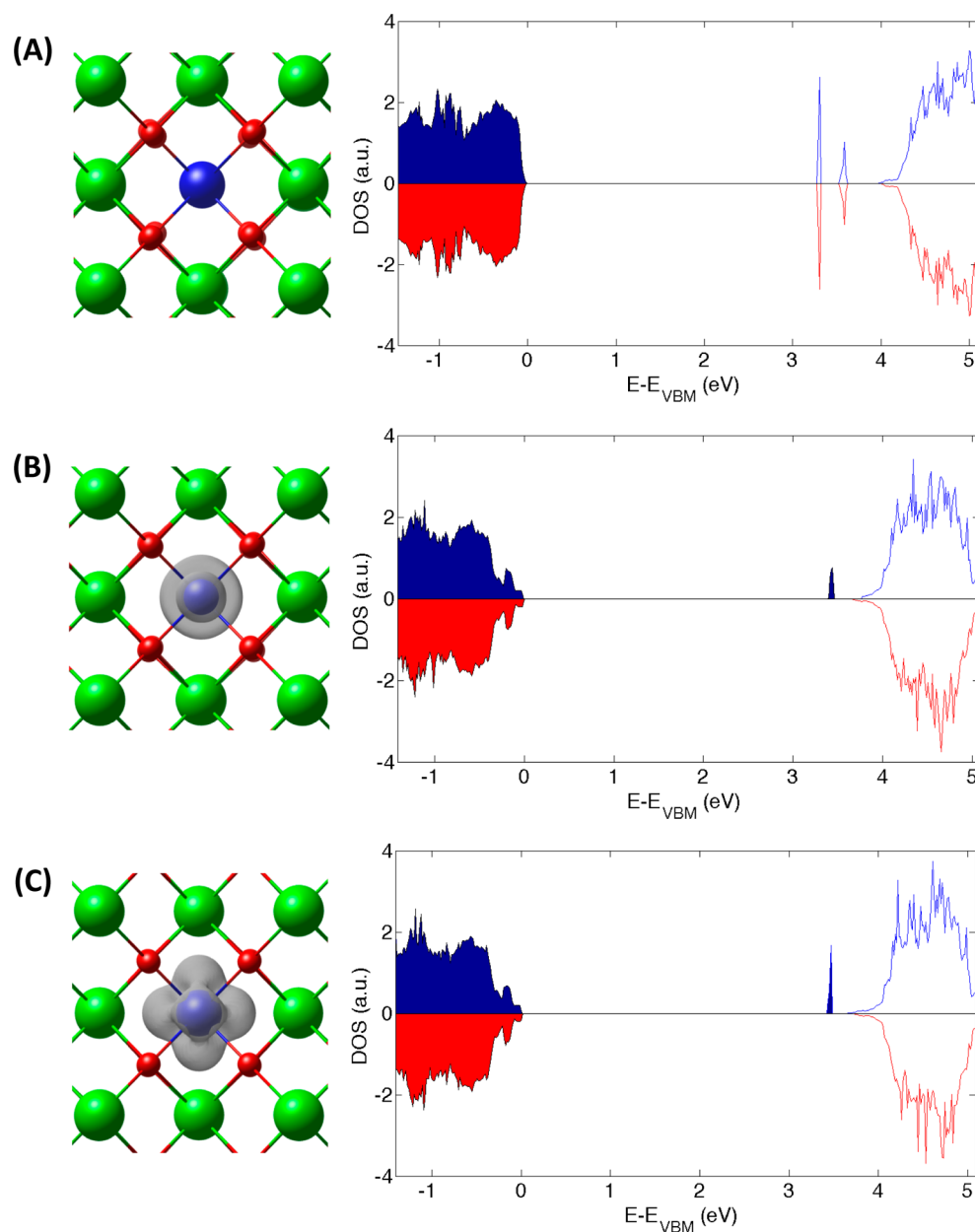
Figure 1. Calculated net spin density distribution of the three achievable charge states of the Nb substitutional defect and the corresponding electronic density of states (DOS). $Nb^{\bullet}_{Zr}$, Nb^x_{Zr}, and Nb'_{Zr} are shown in parts A, B, and C, respectively. Green (large), blue (medium), and red (small) balls represent Zr, Nb, and O ions, respectively. The shown gray isosurfaces of the net spin density distributions were rendered at 0.01 e/Å^3. In the DOS plots, the energy of the edge of the valence band in the defective cell was set to zero and filling indicates occupied states. The gap states in $Nb^{\bullet}_{Zr}$ are unoccupied, whereas those in Nb^x_{Zr} and Nb'_{Zr} are occupied. Positive and negative DOS indicate spin up and spin down, respectively. The atomistic visualizations in parts A, B, and C were rendered using the software VESTA.[47]

combination with the tetrahedron method with Blöchl corrections.[45]

The finite temperature effect is incorporated by including the phonon contribution to the free energy of formation of point defects. The details of calculations are the same as in our recent work,[21] and the code PHONOPY was used to calculate the phonon density of states from the DFT calculated Hessian matrix.[46] The computational results in this work are presented at 1500 K where tetragonal ZrO_2 is thermodynamically stable without doping or stress. The transition temperature from pure monoclinic to tetragonal ZrO_2 is 1440 K.[19]

2.3. Experimental Approach. In order to assess the chemical composition of the oxide near the surface and compare that to the computationally predicted Nb enrichment near the oxide-oxygen gas interface (discussed below), X-ray photoelectron spectroscopy (XPS) measurements were performed on oxidized Zr−2.5 wt % Nb alloy. The polycrystalline Zr−2.5 wt % Nb was purchased from Princeton Scientific Corp. and mechanically polished (last step 0.25 μm). Then, the sample was introduced into an ultrahigh vacuum (UHV) system for surface preparation and in situ measurement upon oxidation (base pressure <3.0 × 10^{-12} atm). The native oxide and other contaminations on the surface were removed by cycles of Ar$^+$ beam sputtering and vacuum annealing at 650 °C. A 1.5 kV acceleration voltage and 20 mA emission current were used during sputtering. After more than five cycles of sputtering and annealing, there was no other peak than Zr and Nb observed in the XPS survey spectrum. Next, the oxide films were grown by oxidation at 300 °C at 2.0 × 10^{-11} atm by exposure to pure oxygen gas in the analysis chamber.

An Omicron EA 125 hemispherical analyzer and Omicron DAR 400 Mg/Al dual anode non-monochromatic X-ray source were used for the angle resolved X-ray photoelectron spectroscopy (AR-XPS) measurements probing the near-surface chemistry of the metal and of the grown zirconium oxide. A key focus was measurement of the Zr 3d and Nb 3d emissions (binding energy from 175 to 211 eV) to determine the atomic ratio between Zr and Nb. The AR-XPS measurements were performed before and after oxidation, by detecting the photoelectrons at 90, 60, and 30°. The XPS measurements were performed in the UHV chamber. An Al K X-ray source (1486.7 eV), operated at 300 W, was used for all the XPS measurements. Peak-fitting and chemical quantification were performed using the CasaXPS 2.3.16 software.

3. RESULTS

In this section, we present the key results based on our theoretical analysis and experimental validation. Our results indicate that Nb exists as a substitutional defect in tetragonal ZrO$_2$ in the oxidation states 3+, 4+, and 5+. The latter is by far the dominant in concentration. Nb^{5+} is charge compensated by V_{Zr}'''' and is present only under oxygen-rich conditions. Our XPS measurements confirmed the presence of Nb in the oxygen-rich part of the oxide where Nb segregation to the near-surface region of the oxide scale grown on Zr−Nb alloy was detected. Nb leads to an increase in V_{Zr}'''' and free electrons and decrease in $V_O^{\bullet\bullet}$ in T-ZrO$_2$. The implications of these results are discussed in the next section.

3.1. Electronic Structure. As discussed in the theoretical approach section, the Nb interstitial defects have a very high formation energy so we limit the discussion to Nb substitutional defects. Table 1 summarizes our charge localization analysis for the three oxidation states of Nb on a Zr site for which we observed correct charge localization on the Nb defect. We observed that Nb can take only 5+, 4+, and 3+ oxidation states on a Zr site. Any additional electrons added to the 3+ oxidation state in order to attain 2+ or less relax into the conduction band. Moreover, we found out that the two electrons localized on Nb^{3+} have a triplet ground state. While these results were obtained using PBE+U, similar conclusions were drawn using the standard PBE functional.

In Figure 1, we show the calculated net spin density distribution and electronic density of states (DOS) for the three achievable charge states of Nb substitutional defects. In

the case of 5+ (Figure 1A), we observe unfilled electronic states in the band gap, whereas for 4+ (Figure 1B) a filled state appears in the band gap together with a net magnetic moment on the Nb ion. In the case of 3+ (Figure 1C), a state in the band gap appears which accounts for two electrons in the triplet spin state.

3.2. Defect Energetics. The formation energy of the possible charge states of the Nb$_{Zr}$ defect as a function of the chemical potential of electrons μ_F is shown in Figure 2. Starting
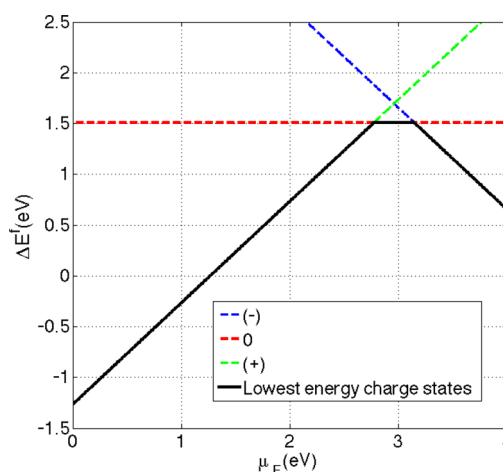
Figure 2. Formation energy of the Nb$_{Zr}$ defect under oxygen-rich conditions (P_{O_2} = 1 atm), as a function of the chemical potential of electrons μ_F. The solid line represents the minimum formation energy over all possible charge states, while dashed lines are the formation energies of the (+), 0, and (−) charge states.

from the edge of the valence band and for a wide range of μ_F in the DFT-calculated band gap, we found Nb$_{Zr}^{\bullet}$ to be the predominant charge state. At 1500 K, under oxygen-rich conditions, μ_F lies in the range of predomination of Nb$_{Zr}^{\bullet}$, as we show in the next subsection. It is important to notice that the Nb$_{Zr}^{\bullet}$ predomination range is still relatively far from the edge of the conduction band, which indicates that free electrons may not be the main charge compensation mechanism and negative native defects are needed to compensate Nb$_{Zr}^{\bullet}$. Our calculation of the Kröger−Vink diagram shows that V_{Zr}'''' is the main compensator, as we discuss below.

Following the definition of eq 5, we calculated the binding energy of the Nb$_{Zr}^q$ defect against dissociation to its constituents and the results are summarized in Table 2. All three stable

**Table 2. Calculated Binding Energies and Dissociation Products of the Nb Substitutional Defects**

defect	Nb$_{Zr}'$	Nb$_{Zr}^x$	Nb$_{Zr}^{\bullet}$
E_{bind} (eV)	−5.2	−6.6	−7.7
dissociation products	Nb$_i^{\bullet\bullet\bullet}$ + V_{Zr}''''	Nb$_i^{\bullet\bullet\bullet\bullet}$ + V_{Zr}''''	Nb$_i^{\bullet\bullet\bullet\bullet\bullet}$ + V_{Zr}''''

charge states of this defect were found to be thermodynamically bound (negative binding energy). The easiest dissociation pathway for each charge state is also listed in Table 2.

3.3. Calculated Kröger−Vink Diagram and Comparison with Experiments. Following the theoretical framework presented in section 2.1, the Kröger−Vink diagram for Nb containing T-ZrO$_2$ was constructed and compared to the previously computed defect equilibria for pure T-ZrO$_2$.[21] The results are presented in Figure 3. In the high P_{O_2} range, the

20126

dx.doi.org/10.1021/jp504874v | J. Phys. Chem. C 2014, 118, 20122−20131
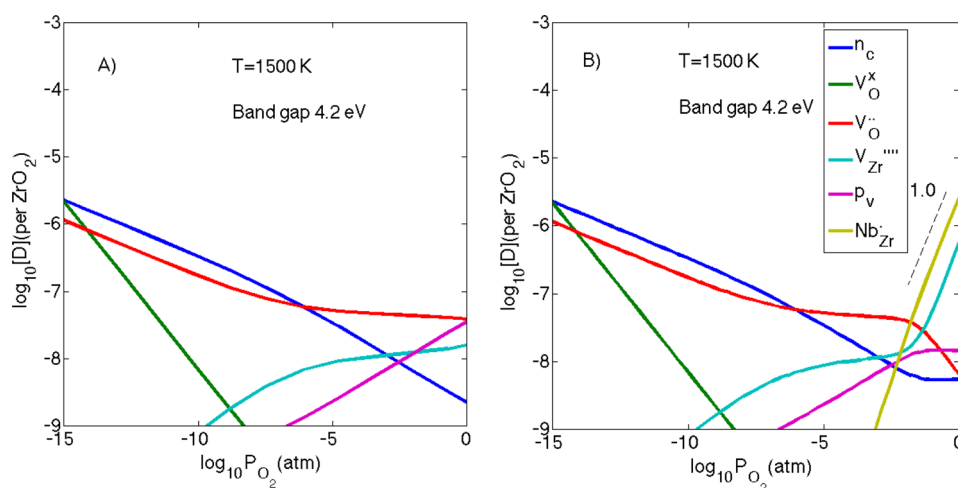
Figure 3. Calculated Kröger−Vink diagram for tetragonal ZrO$_2$ at 1500 K. (A) Undoped case (reproduction of the results in ref 21). (B) Nb-doped case. Ionic defects are denoted using Kröger−Vink notation. Conduction band electrons and valence band holes are denoted by n$_c$ and p$_v$, respectively. The dashed line in part B indicates a slope of +1.0. Defects with a concentration less than 10^{-9} per ZrO$_2$ are not shown.
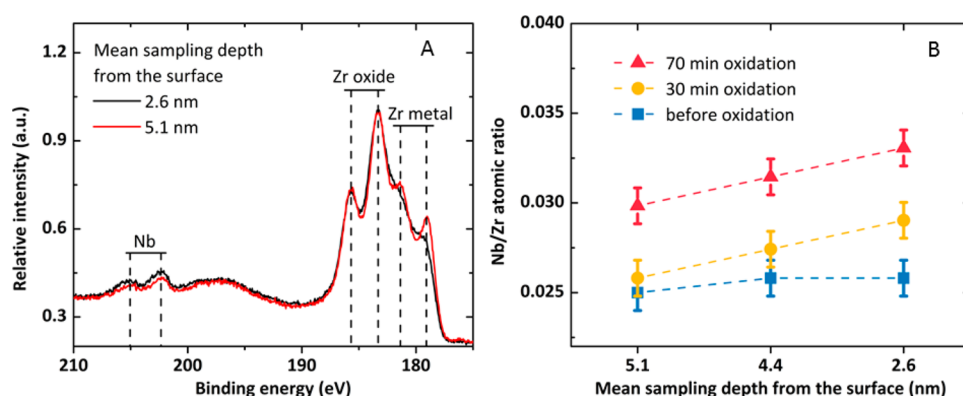
Figure 4. (A) Zr 3d and Nb 3d X-ray photoelectron spectra measured after 30 min of oxidation at detection angles of 30 and 90° (probing depth 2.6 and 5.1 nm, respectively). (B) Nb/Zr ratio quantified from the Zr 3d and Nd 3d X-ray photoelectron spectra measured as a function of detection angle (depth) and time of oxidation. The near-surface data shows more Nb enrichment.

positive charge introduced into the system by the creation of Nb$_{Zr}^{\bullet}$ is compensated by an increase in the concentration of conduction band electrons n$_c$ and of V$_{Zr}''''$, and by a drop in the concentration of V$_O^{\bullet\bullet}$. Our results suggest that the increase in V$_{Zr}''''$ is the dominant charge compensation mechanism for Nb$_{Zr}^{\bullet}$. This is in contrast to prior suggestions which attributed the charge compensation to oxygen related defects without regard to zirconium vacancies.[23] At low P$_{O_2}$, the difference between the defect equilibria in undoped and Nb-doped zirconia is negligible. This is indeed expected, since the lattice site through which Nb dissolves in zirconia is the cation site. The implication here for the corrosion of zirconium alloys is that Nb does not dissolve in zirconia in the oxygen-poor region, that is close to the metal oxide interface. Instead, it dissolves in the oxygen-rich part of the oxide close to the surface (oxide/oxidizing environment interface).

The tetragonal phase of ZrO$_2$ is stable at typical nuclear reactor operation temperatures (∼600 K) mainly by virtue of the biaxial stress that arises due to the lattice mismatch between the oxide and the underlying zirconium alloy.[20] Our simulation results represent the defect equilibria in tetragonal zirconia at 1500 K. This high temperature in the simulations is necessary in the absence of stress effects to stabilize the tetragonal phase in the simulations. However, even in the presence of stress and

at reactor temperatures, we still believe that the picture predicted by our simulations at 1500 K is qualitatively valid. That is, Nb dissolves in zirconia in the high P$_{O_2}$ region close to the oxide/environment interface and is absent in the low P$_{O_2}$ region near the metal/oxide interface. The reason for the validity of this picture is that Nb predominantly dissolves as a substitutional defect on the cation site with almost zero contribution from interstitial sites. To confirm this, in our XPS measurements, the Nb and Zr contents were quantified at various depths from the surface of the oxide by changing the detection angle. The resulting Nb/Zr atomic ratio at different probing depths indicates whether Nb indeed enriches at the oxygen-rich region of the zirconia, that is, near the surface of the oxide as the metal oxidizes. According to the inelastic mean free path of photoelectrons, about 95% of the signal comes from the top 7.2, 6.2, or 3.6 nm when the detection angle is 90, 60, or 30°, respectively. There is no evidence for Nb enrichment on the 2.5% Nb−Zr alloy surface before oxidation, as shown in Figure 4B. With oxidation times up to 70 min, an increase in the Nb/Zr atomic ratio was found at/near the surface (0.033 compared to 0.025 before oxidation), as in Figure 4A and B. This experimental evidence to the segregation of Nb toward the near surface region of the oxide validates well

the computational prediction of an increasing amount of $Nb_{Zr}^{\bullet}$ in the oxygen-rich region of T-ZrO_2 shown in Figure 3B.

4. DISCUSSION

4.1. Charge State of Nb in Tetragonal ZrO_2 and Charge Compensation Mechanism. Our theoretical model showed that Nb dissolves in oxygen-rich T-ZrO_2 in 5+ charge state on a Zr lattice site, that is, $Nb_{Zr}^{\bullet}$. The defect $Nb_{Zr}^{\bullet}$ is typically what is assumed in explaining the corrosion of Zr−Nb alloys[23] or even in atomistic simulation of Nb-doped zirconia.[24] In ref 23, the defect Nb_{Zr}'' (Nb^{2+}) was also assumed to be present in the oxide layer of the Zr−Nb alloy in the oxygen-poor part of the oxide. However, our DFT calculations indicate that localizing an electron on Nb^{3+} to form Nb^{2+} is not possible. Moreover, even if Nb_{Zr}'' exists in the oxide layer, it has to exist predominantly in the oxygen-rich part of the oxide, since it is a substitutional defect on the Zr site.

More importantly, to the best of our knowledge, the charge compensation mechanism of $Nb_{Zr}^{\bullet}$ in the dilute limit in tetragonal zirconia discussed in the literature never took into account the role of native cation vacancies. In classical atomistic simulations, the compensator is typically assumed to be another extrinsic dopant such as Y^{3+}.[24] In interpreting the experimental results of ref 23, Hobbs et al. assumed the depression of $V_O^{\bullet\bullet}$ as the mere compensation mechanism. While the latter assumption was confirmed in our calculated Kröger−Vink diagram, we also showed that the predominant compensator is V_{Zr}''''.

4.2. Implications on Corrosion Kinetics. The presence of Nb alters both the ionic and electronic defect concentrations in T-ZrO_2. Therefore, the expected effect of Nb on corrosion kinetics is both through the diffusion of oxygen and cation vacancies and through the charge transfer at the surface. In the oxygen-rich medium near the oxide/water or oxide/gas interface, a drop in the oxygen vacancy concentration acts to limit the availability of the key mediator to oxygen diffusion. In the same region, the increased concentration of electrons in the conduction band would increase the electron conduction rate and facilitate charge transfer at the surface of the oxide. Below we compare these two competing factors quantitatively to decide whether Nb should increase the corrosion resistance or not based on intrinsic properties of the zirconia passive film.

The increase in conduction band electrons, n_c, in high P_{O_2} due to the added Nb is shown in Figure 5. At the highest P_{O_2}, there is an increase of more than twice in the concentration of n_c in the presence of Nb. This relatively small change in n_c is anticipated given that the compensation of $Nb_{Zr}^{\bullet}$ is achieved mainly via the native ionic defects, specifically by V_{Zr}''''. An increase in n_c would provide more electrons available for transfer on the surface to the oxidizing species such as oxygen molecules,[48,49] thereby increasing the corrosion rate. It was shown previously that the reduction and dissociation of the oxygen molecule, electron transfer may not be necessary for the reduction of water at the zirconia surface.[50] In that case, the increase in n_c would contribute to the electron conduction rate in the bulk and to the reduction of protons (byproducts of water splitting), leading to hydrogen gas evolution at the surface. Thus, the increase in n_c induced by Nb suggests that Nb can potentially, and detrimentally, accelerate the corrosion kinetics of Zr alloys. However, the complete picture of the Nb effect requires careful examination of Nb impact on also the concentrations of ionic defects.
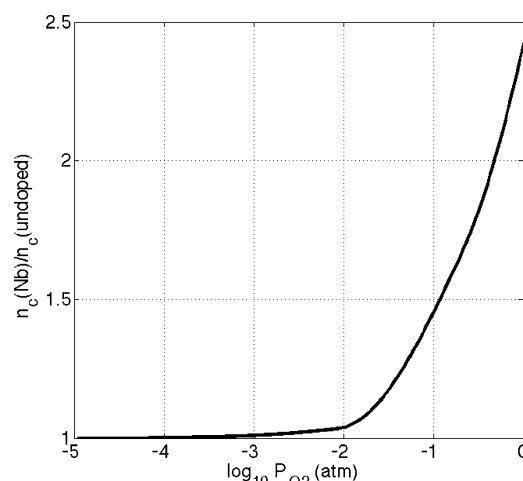
Figure 5. Relative change in the concentration of conduction band electrons, n_c, in the Nb-doped tetragonal ZrO_2 compared to the undoped tetragonal ZrO_2 at 1500 K.

Under oxygen-rich conditions and due to Nb doping in tetragonal ZrO_2, the relative decrease in the concentration of $V_O^{\bullet\bullet}$ and the relative increase in the concentration of V_{Zr}'''' are shown in Figure 6. These point defects mediate the transport of
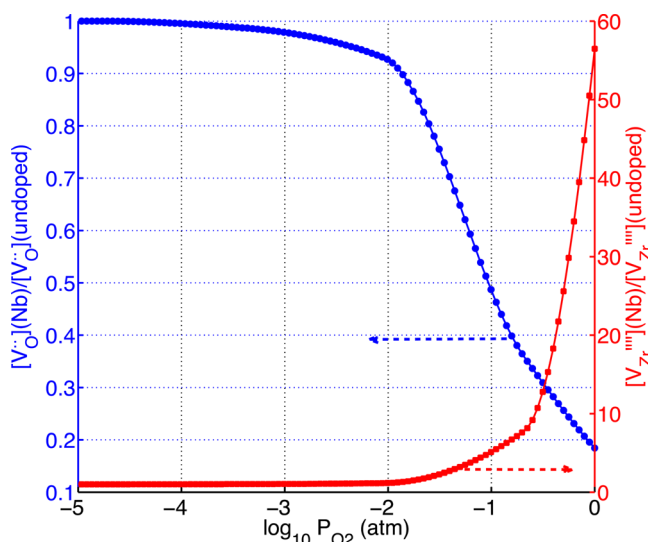
Figure 6. Relative change in the concentrations of $V_O^{\bullet\bullet}$ and V_{Zr}'''' in the Nb-doped tetragonal ZrO_2 compared to the undoped tetragonal ZrO_2 at 1500 K.

oxygen from the oxide/environment interface to the metal/oxide interface and the transport of zirconium from the metal/oxide interface to the oxide/environment interface, respectively. Both of these transport processes are important in the oxidation of zirconium.[6] The self-diffusivity of oxygen or of zirconium arises from the contribution of all the defects of oxygen or zirconium that can exist in ZrO_2. Each defect contributes to the self-diffusivity via its concentration and migration (mobility).[51] In the dilute limit considered in this work, it is reasonable to assume that the migration barriers of the defects are not influenced by Nb doping or by the variations of P_{O_2}. Thus, the effect of Nb on the self-diffusivity of O and Zr will be accomplished through its effect on the concentration of O and Zr defects. In Figure 6 and at the highest P_{O_2} considered, the

concentration of $V_O^{\bullet\bullet}$ drops by 80% because of Nb. Consequently, oxygen self-diffusivity is expected to drop by 80% as well. We note here that, at high P_{O_2} and at the temperature considered here 1500 K, oxygen self-diffusivity is predominantly controlled by $V_O^{\bullet\bullet}$, as we showed in our previous work.[51] Figure 6 also shows that the concentration of V_{Zr}'''' is elevated by about 60 times at 1 atm as a result of Nb point defects in T-ZrO$_2$. Following the same argument above, the Zr cation transport would be accelerated by about 60 times in this case. However, the diffusivity of oxygen in zirconia is faster by many orders of magnitude compared to that of the zirconium in zirconia scale that grows on zirconium alloys.[52,53] For example, at 500 K in monoclinic ZrO$_2$, the diffusion coefficients of zirconium and oxygen are 10^{-20} and 10^{-12} cm^2 s^{-1}, respectively.[54] Therefore, we believe that the 60 times increase in the concentration of V_{Zr}'''' in the presence of Nb is not large enough to render V_{Zr}'''' a mobile defect in comparison with $V_O^{\bullet\bullet}$.

In order to understand the net effect of Nb on the corrosion kinetics of zirconium alloys, we recall here the fact that the oxidation of zirconium is inward.[14] That is, oxygen is much more mobile than zirconium and diffuses from the surface of the oxide toward the metal/oxide interface in order to oxidize the underlying metal. This process takes place via the diffusion of $V_O^{\bullet\bullet}$ from the metal/oxide interface to the oxide surface. In order to maintain charge neutrality and to close the cycle of the corrosion reaction, electrons have to transport from the metal/oxide interface toward the oxide surface. There is a controversy in the literature over which of these transport processes is the rate limiting: oxygen diffusion or electron transport.[14] Our results indicate that Nb increases conduction band electrons and decreases $V_O^{\bullet\bullet}$, at comparable magnitude of relative changes in each. Thus, if oxygen vacancies are the rate limiting defects, then Nb slows down the corrosion kinetics. Conversely, if free electrons are the rate limiting defects, then Nb accelerates corrosion kinetics, an undesirable outcome. The rich and complex change in the defect chemistry of T-ZrO$_2$ generated by Nb doping provides an explanation for the inconclusive experimental results regarding its impact on the corrosion kinetics, as discussed in the Introduction. Although these comparisons were conducted on the basis of the calculated defect equilibria at 1500 K without stress effects, we believe that the qualitative trends still hold at lower temperatures. The next step in future work would be the explicit inclusion of stress effects and calculating the defect equilibria in T-ZrO$_2$ at lower temperatures.

On the basis of the variations in the point defect concentrations discussed above, it is possible to calculate an integral quantity that is representative of the overall defect equilibria. That is, the off-stoichiometry, x. This quantity is experimentally measurable and was measured previously for undoped zirconia.[55] From the constructed Kröger–Vink diagram, x was calculated as

$$x = \frac{2 + \sum_q [O_i^q] - \sum_q [V_O^q]}{1 + \sum_q [Zr_i^q] - \sum_q [V_{Zr}^q] - \sum_q [Nb_{Zr}^q]} - 2 \tag{6}$$

In Figure 7, we present the calculated off-stoichiometry in Nb-doped T-ZrO$_2$ at 1500 K. Contrary to undoped T-ZrO$_2$ which was found to always be hypostoichiometric ($x < 0$) both theoretically[21] and experimentally,[55] our results indicate that Nb-doped T-ZrO$_2$ can exhibit hyperstoichiometry under oxygen-rich conditions. This is mainly due to the creation of
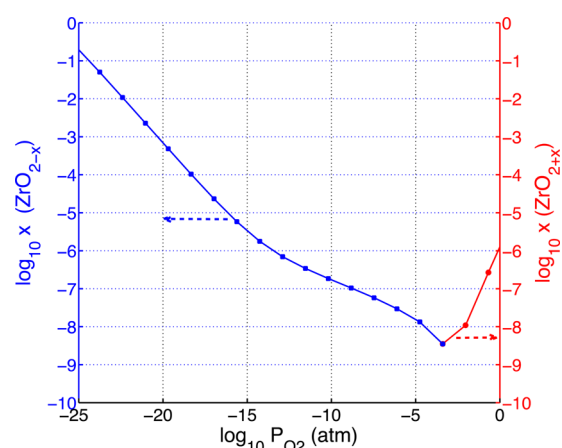
Figure 7. Calculated off-stoichiometry, x, in Nb-doped tetragonal ZrO$_2$ at 1500 K. At P_{O_2} lower than 10^{-4} atm, the oxide is hypostoichiometric, while, above 10^{-4} atm, the oxide is hyperstoichiometric due to the presence of cation vacancies.

zirconium vacancies. As P_{O_2} decreases and at about 10^{-4} atm, the oxide becomes hypostoichiometric by virtue of the increase in the concentration of $V_O^{\bullet\bullet}$. Our calculation for x in Nb-doped tetragonal ZrO$_2$ motivates future experimental work for validation of our predictions.

5. CONCLUSION

In this work, we presented a thorough DFT-based analysis of the effect of Nb on the defect equilibria in tetragonal ZrO$_2$, and partly validated our predictions by XPS measurements. We showed that Nb dissolves in T-ZrO$_2$ in the form of a substitutional defect on the Zr site in the oxidation states 3+, 4+, and 5+, with 5+ being the predominant one. Charge compensation of Nb$_{Zr}^{\bullet}$ is achieved mainly by V_{Zr}''''. Moreover, Nb dissolution in T-ZrO$_2$ takes place only under oxygen-rich conditions, which is representative of the oxide/water (oxide/oxygen gas) interface in a corrosion scenario. This finding was confirmed by our XPS measurements where Nb enrichment near the surface compared to the bulk of the oxide scale grown on Zr−Nb alloy was detected.

Under oxygen-rich conditions, Nb doping results in an increase in the concentration of V_{Zr}'''' and of free electrons and a decrease in the concentration of $V_O^{\bullet\bullet}$. The very slow mobility of V_{Zr}'''' excludes it from playing an important role in the corrosion kinetics. The diffusivity of $V_O^{\bullet\bullet}$ and the conductivity of free electrons are both proposed in the literature to be important in determining the oxidation kinetics of Zr. The changes in the concentrations of those two defects induced by Nb in T-ZrO$_2$ are comparable. Thus, depending on the rate limiting defect, $V_O^{\bullet\bullet}$ vs free electrons, Nb could decelerate or accelerate the corrosion kinetics. The rich and complex change in the defect chemistry of T-ZrO$_2$ generated by Nb doping provides an explanation for the inconclusive experimental results in the literature regarding its impact on the corrosion kinetics. Finally, we observed that the net effect of the defect equilibria due to the introduction of Nb is the possibility of attaining a hyperstoichiometric T-ZrO$_2$ under oxygen-rich conditions. This result is amenable to future experimental validation.

A future refinement of our work would be to explicitly account for the effect of stress on the defect equilibria in Nb-doped T-ZrO$_2$. This is needed to achieve a more quantitative comparison with the actual conditions to which T-ZrO$_2$ is

exposed in nuclear reactors. The results and analyses presented here are broadly applicable in other fields such as catalysis and fuel cells where the effects of doping metal oxides are consequential.

■ AUTHOR INFORMATION

Corresponding Author

*E-mail: byildiz@mit.edu. Mailing address: Massachusetts Institute of Technology, 77 Massachusetts Avenue, Cambridge, Rm: 24-210, MA 02139, USA. Phone: +1-617-258-4009.

Notes

The authors declare no competing financial interest.

■ REFERENCES

(1) Chevalier, J.; Gremillard, L.; Virkar, A. V.; Clarke, D. R. The Tetragonal-Monoclinic Transformation in Zirconia: Lessons Learned and Future Trends. *J. Am. Ceram. Soc.* **2009**, *92*, 1901−1920.

(2) Chroneos, A.; Yildiz, B.; Tarancon, A.; Parfitt, D.; Kilner, J. A. Oxygen Diffusion in Solid Oxide Fuel Cell Cathode and Electrolyte Materials: Mechanistic Insights from Atomistic Simulations. *Energy Environ. Sci.* **2011**, *4*, 2774−2789.

(3) Schulz, U.; Leyens, C.; Fritscher, K.; Peters, M.; Saruhan-Brings, B.; Lavigne, O.; Dorvaux, J.-M.; Poulain, M.; Mévrel, R.; Caliez, M. Some Recent Trends in Research and Technology of Advanced Thermal Barrier Coatings. *Aerosp. Sci. Technol.* **2003**, *7*, 73−80.

(4) Yilmazbayhan, A.; Breval, E.; Motta, A. T.; Comstock, R. J. Transmission Electron Microscopy Examination of Oxide Layers Formed on Zr Alloys. *J. Nucl. Mater.* **2006**, *349*, 265−281.

(5) Chen, Y.; Urquidi-Macdonald, M.; Macdonald, D. D. The Electrochemistry of Zirconium in Aqueous Solutions at Elevated Temperatures and Pressures. *J. Nucl. Mater.* **2006**, *348*, 133−147.

(6) Macdonald, D.; Englehardt, G. The Point Defect Model for Bi-Layer Passive Films. *ECS Trans.* **2010**, *28*, 123−144.

(7) Cales, B. Zirconia as a Sliding Material: Histologic, Laboratory, and Clinical Data. *Clin. Orthop. Relat. Res.* **2000**, *379*, 94.

(8) Denry, I.; Kelly, J. R. State of the Art of Zirconia for Dental Applications. *Dent. Mater.* **2008**, *24*, 299−307.

(9) Shluger, A. L.; Foster, A. S.; Gavartin, J. L.; Sushko, P. V. In *Nano and Giga Challenges in Microelectronics*; Greer, J., Korkin, A., Labanowski, J., Eds.; Elsevier: Amsterdam, The Netherlands, 2003.

(10) Guo, X. Property Degradation of Tetragonal Zirconia Induced by Low-Temperature Defect Reaction with Water Molecules. *Chem. Mater.* **2004**, *16*, 3988−3994.

(11) Hull, S. Superionics: Crystal Structures and Conduction Processes. *Rep. Prog. Phys.* **2004**, *67*, 1233.

(12) Kushima, A.; Yildiz, B. Oxygen Ion Diffusivity in Strained Yttria Stabilized Zirconia: Where Is the Fastest Strain? *J. Mater. Chem.* **2010**, *20*, 4809−4819.

(13) Bai, X.-M.; Zhang, Y.; Tonks, M. R. Strain Effects on Oxygen Transport in Tetragonal Zirconium Dioxide. *Phys. Chem. Chem. Phys.* **2013**, *15*, 19438−19449.

(14) Cox, B. Some Thoughts on the Mechanisms of in-Reactor Corrosion of Zirconium Alloys. *J. Nucl. Mater.* **2005**, *336*, 331−368.

(15) Yilmazbayhan, A.; Silva, M. G. d.; Motta, A.; Kim, H.-G.; Jeong, Y. H.; Park, J.-Y.; Comstock, R.; Lai, B.; Cai, Z. Characterization of Oxides Formed on Model Zirconium Alloys in 360°C Water Using Micro-Beam Synchrotron Radiation. *Proc. Int. Conf. Environ. Degrad. Mater. Nucl. Power Syst.—Water React., 12th* **2005**, *12*, 201−212.

(16) Dali, Y.; Tupin, M.; Bossis, P.; Pijolat, M. Effect of Alloying Elements on the Oxidation Kinetics of Zirconium Based Alloys under High Pressure Steam. *NACE Int.* **2007**, 07601.

(17) Yueh, H. K.; Kesterson, R. L.; Comstock, R. J.; Shah, H. H.; Colburn, D. J.; Dahlback, M.; Hallstadius, L. Improved Zirlo Cladding Performance through Chemistry and Process Modifications. *J. ASTM Int.* **2005**, *2*, 1−10.

(18) Macdonald, D. D. Passivity - the Key to Our Metals-Based Civilization. *Pure. Appl. Chem.* **1999**, *71*, 951−978.

(19) Green, D. J.; Hannik, R. H.; Swanik, M. V. *Transformation Toughening of Ceramics*; CRC Press: Boca Raton, FL, 1989.

(20) Kim, Y.-S.; Jeong, Y.-H.; Jang, J.-N. Stress Measurements During Thin Film Zirconium Oxide Growth. *J. Nucl. Mater.* **2011**, *412*, 217−220.

(21) Youssef, M.; Yildiz, B. Intrinsic Point-Defect Equilibria in Tetragonal ZrO_2: Density Functional Theory Analysis with Finite-Temperature Effects. *Phys. Rev. B* **2012**, *86*, 144109.

(22) Froideval, A.; Degueldre, C.; Segre, C. U.; Pouchon, M. A.; Grolimund, D. Niobium Speciation at the Metal/Oxide Interface of Corroded Niobium-Doped Zircaloys: A X-Ray Absorption near-Edge Structure Study. *Corros. Sci.* **2008**, *50*, 1313−1320.

(23) Hobbs, L. W.; Rosen, V. B.; Mangin, S. P.; Treska, M.; Hunter, G. Oxidation Microstructures and Interfaces in the Oxidized Zirconium Knee. *Int. J. Appl. Ceram. Technol.* **2005**, *2*, 221−246.

(24) Sakib Khan, M.; Saiful Islam, M.; R. Bates, D. Cation Doping and Oxygen Diffusion in Zirconia: A Combined Atomistic Simulation and Molecular Dynamics Study. *J. Mater. Chem.* **1998**, *8*, 2299−2307.

(25) Van de Walle, C. G.; Neugebauer, J. First-Principles Calculations for Defects and Impurities: Applications to Iii-Nitrides. *J. Appl. Phys.* **2004**, *95*, 3851−3879.

(26) Makov, G.; Payne, M. C. Periodic Boundary Conditions in *Ab Initio* Calculations. *Phys. Rev. B* **1995**, *51*, 4014−4022.

(27) Youssef, M.; Yildiz, B. Hydrogen Defects in Tetragonal ZrO_2 Studied Using Density Functional Theory. *Phys. Chem. Chem. Phys.* **2014**, *16*, 1354−1365.

(28) Chase, M. W., Jr. *Nist-Janaf Thermochemical Tables*; American Institute of Physics: Woodbury, NY, 1998.

(29) Cox, B.; Wong, Y. M. A Hydrogen Uptake Micro-Mechanism for Zr Alloys. *J. Nucl. Mater.* **1999**, *270*, 134−146.

(30) McComb, D. W. Bonding and Electronic Structure in Zirconia Pseudopolymorphs Investigated by Electron Energy-Loss Spectroscopy. *Phys. Rev. B* **1996**, *54*, 7094−7102.

(31) Kofstad, P.; Ruzicka, D. J. On the Defect Structure of ZrO_2 and Hfo_2. *J. Electrochem. Soc.* **1963**, *110*, 181−184.

(32) Oba, F.; Togo, A.; Tanaka, I.; Paier, J.; Kresse, G. Defect Energetics in Zno: A Hybrid Hartree-Fock Density Functional Study. *Phys. Rev. B* **2008**, *77*, 245202.

(33) Shrader, D.; Khalil, S. M.; Gerczak, T.; Allen, T. R.; Heim, A. J.; Szlufarska, I.; Morgan, D. Ag Diffusion in Cubic Silicon Carbide. *J. Nucl. Mater.* **2011**, *408*, 257−271.

(34) Bader, R. F. W. A Quantum Theory of Molecular Structure and Its Applications. *Chem. Rev.* **1991**, *91*, 893−928.

(35) Tang, W.; Sanville, E.; Henkelman, G. A Grid-Based Bader Analysis Algorithm without Lattice Bias. *J. Phys.: Condens. Matter* **2009**, *21*, 084204.

(36) Kresse, G.; Joubert, D. From Ultrasoft Pseudopotentials to the Projector Augmented-Wave Method. *Phys. Rev. B* **1999**, *59*, 1758−1775.

(37) Perdew, J. P.; Burke, K.; Ernzerhof, M. Generalized Gradient Approximation Made Simple. *Phys. Rev. Lett.* **1996**, *77*, 3865−3868.

(38) Perdew, J. P.; Burke, K.; Ernzerhof, M. Generalized Gradient Approximation Made Simple [Phys. Rev. Lett. 1996, 77, 3865]. *Phys. Rev. Lett.* **1997**, *78*, 1396−1396.

(39) Kresse, G.; Hafner, J. *Ab Initio* Molecular Dynamics for Liquid Metals. *Phys. Rev. B* **1993**, *47*, 558−561.

(40) Kresse, G.; Hafner, J. *Ab Initio* Molecular-Dynamics Simulation of the Liquid-Metal−Amorphous-Semiconductor Transition in Germanium. *Phys. Rev. B* **1994**, *49*, 14251−14269.

(41) Kresse, G.; Furthmüller, J. Efficiency of Ab-Initio Total Energy Calculations for Metals and Semiconductors Using a Plane-Wave Basis Set. *Comput. Mater. Sci.* **1996**, *6*, 15−50.

(42) Kresse, G.; Furthmüller, J. Efficient Iterative Schemes for *Ab Initio* Total-Energy Calculations Using a Plane-Wave Basis Set. *Phys. Rev. B* **1996**, *54*, 11169−11186.

(43) Hautier, G.; Ong, S. P.; Jain, A.; Moore, C. J.; Ceder, G. Accuracy of Density Functional Theory in Predicting Formation Energies of Ternary Oxides from Binary Oxides and Its Implication on Phase Stability. *Phys. Rev. B* **2012**, *85*, 155208.

(44) Dudarev, S. L.; Botton, G. A.; Savrasov, S. Y.; Humphreys, C. J.; Sutton, A. P. Electron-Energy-Loss Spectra and the Structural Stability of Nickel Oxide:An Lsda+U Study. *Phys. Rev. B* **1998**, *57*, 1505−1509.

(45) Blöchl, P. E.; Jepsen, O.; Andersen, O. K. Improved Tetrahedron Method for Brillouin-Zone Integrations. *Phys. Rev. B* **1994**, *49*, 16223−16233.

(46) Togo, A.; Oba, F.; Tanaka, I. First-Principles Calculations of the Ferroelastic Transition between Rutile-Type and $Cacl_2$ -Type Sio2 at High Pressures. *Phys. Rev. B* **2008**, *78*, 134106.

(47) Momma, K.; Izumi, F. Vesta 3 for Three-Dimensional Visualization of Crystal, Volumetric and Morphology Data. *J. Appl. Crystallogr.* **2011**, *44*, 1272−1276.

(48) Jung, W.; Tuller, H. L. A New Model Describing Solid Oxide Fuel Cell Cathode Kinetics: Model Thin Film $Srti_{1-x}fe_xo_{3-\Delta}$ Mixed Conducting Oxides−a Case Study. *Adv. Energy Mater.* **2011**, *1*, 1184−1191.

(49) Greiner, M. T.; Chai, L.; Helander, M. G.; Tang, W.-M.; Lu, Z.-H. Transition Metal Oxide Work Functions: The Influence of Cation Oxidation State and Oxygen Vacancies. *Adv. Funct. Mater.* **2012**, *22*, 4557−4568.

(50) Garcia, J. C.; Deskins, N. A. Detailing Ionosorption over TiO_2, ZrO_2, and HfO_2 from First Principles. *J. Phys. Chem. C* **2012**, *116*, 16573−16581.

(51) Youssef, M.; Yildiz, B. Predicting Self-Diffusion in Metal Oxides from First Principles: The Case of Oxygen in Tetragonal ZrO_2. *Phys. Rev. B* **2014**, *89*, 024105.

(52) Cox, B.; Pemsler, J. P. Diffusion of Oxygen in Growing Zirconia Films. *J. Nucl. Mater.* **1968**, *28*, 73−78.

(53) Whitton, J. L. The Measurement of Ionic Mobilities in the Anodic Oxides of Tantalum and Zirconium by a Precision Sectioning Technique. *J. Electrochem. Soc.* **1968**, *115*, 58−61.

(54) Degueldre, C.; Amato, A.; Bart, G. Muon Spin Relaxation Measurements on Zirconia Samples. *Scr. Mater.* **2006**, *54*, 1211−1216.

(55) Carniglia, S. C.; Brown, S. D.; Schroeder, T. F. Phase Equilibria and Physical Properties of Oxygen-Deficient Zirconia and Thoria. *J. Am. Ceram. Soc.* **1971**, *54*, 13−17.

20131

dx.doi.org/10.1021/jp504874v | *J. Phys. Chem. C* 2014, 118, 20122−20131